ELSEVIER

Contents lists available at ScienceDirect

Materials Science & Engineering A

journal homepage: www.elsevier.com/locate/msea





Short range ordering and strengthening in CoCrNi medium-entropy alloy

Q. Zhang^a, X. Jin^a, X.H. Shi^a, J.W. Qiao^{a,*}, P.K. Liaw^b

- ^a Laboratory of High-Entropy Alloys, College of Materials Science and Engineering, Taiyuan University of Technology, Taiyuan, 030024, China
- b Department of Materials Science and Engineering, The University of Tennessee, Knoxville, TN, 37996-2200, USA

ARTICLE INFO

Keywords: High-entropy alloys Nanoindentation Incipient plasticity Bimodal distribution Slow cooling

ABSTRACT

The CrCoNi medium-entropy alloy is found to exhibit higher incipient plastic strength by slow cooling after the homogenization treatment. Compared with water quenching, this strengthening originates from the inconsistency of the residual stress and short-range orderings (SROs). By deconvolution of the density distribution of the critical shear stress for the first pop-in, two peaks corresponding to homogeneous and heterogeneous dislocation nucleation, respectively, are suggested. Combining the mean, areal fraction, and activation volume of the two peaks, the roles of residual stress and SROs were quantified. Here, for SRO that increases the critical shear stress for heterogeneous and homogeneous nucleation by 22.4% and 39.9%, the residual stress is negligible for the 2.1% strengthening of both. As a result, slow cooling promotes the formation of SRO in CrCoNi, which is of immense benefit to elevate its properties.

There has seen an ongoing rush worldwide in the studies on highentropy alloys (HEAs) and their distribution of alloy compositions [1-10]. As a new class of metallic materials with equimolar multicomponents, it is considered that HEAs are in a completely disordered state, as well as their derivatives (e.g., medium-entropy alloys, MEAs). In the light of the present studies, however, different types of atoms possess various site preferences in different sublattice environments, which drives the generation of short-range orderings (SROs) at nm length scales [2,11-13]. Of special note is that these SROs are subjected to processing conditions such as cooling rate which affects the time at certain temperatures [1.14]. As the temperature goes down, the site preferences of various atoms become apparent, compared to the weak propensity for chemical ordering at elevated temperatures. To date, several works involving experimental and theoretical findings on the formation and characterization of SROs have been reported [2,15,16]. Furthermore, the presence of such nanoscale SROs in HEAs will increase the activation energy barrier for dislocation-mediated plasticity [17], which, in turn, will enhance the work-hardening ability and strain-rate sensitivity of the alloys [18].

To detect the intensity contribution of the presence of chemical inhomogeneous at nanometric scales, the dissection of deformation mechanisms at considerable length scales is an optional breakthrough [19,20]. As this is the case, the elastic-to-plastic transition examined by an nanoindentation technique is ideally suited, which manifests as the first displacement burst (or pop-in) on the load-displacement (*P-h*) curve

when the load-controlled mode is implemented [19,21]. For an indenter with a small tip radius, the deformed volume when the incipient plasticity occurs can even reach a few nm³. Insight into the nature of the pop-in events, dislocation nucleation and/or activation of existing dislocations is at the mercy of the local fluctuation of chemistry to some extent [22]. Taking the bimodality of the cumulative distributions of incipient strengths for metallic glasses (MGs) [23,24] as a reference, Zhao et al. [22] examined the bimodality of statistical distributions in HEAs, and two types of dislocation-nucleation mechanisms were proposed and analyzed.

To investigate the vital effect of site preferences on the deformation behavior of multi-principal elements alloys, CoCrNi MEAs with different cooling methods after heat treatments were selected and studied. By reason of inequal cooling rates will cause discrepant residual stresses in the alloys, pure Ni is feasible as a reference. In the present work, Ni and CoCrNi were prepared by arc-melting under an argon atmosphere. The purity of raw materials is at least 99.9 wt percent. The ingots were flipped and remelted at least four times to promote chemical homogeneity, followed by drop casting into a mold with a thickness of 6 mm. Ascast Ni and CoCrNi were hot-rolled at 900 °C for a 50%-reduction ratio. Afterwards, they were encapsulated in a quartz tube and filled with high-purity argon after deeply vacuuming to 2×10^{-2} mbar, and then homogenized at 1200 °C for 24 h, followed by water-quenching and furnace-cooling, respectively. From here on, water-quenched and furnace-cooled samples are described with the suffixes "-w" and "-f,"

E-mail address: qiaojunwei@gmail.com (J.W. Qiao).

^{*} Corresponding author.

respectively. Before nanoindentation experiments, all the specimens were mechanically polished first, followed by electropolishing (a solution of 70% methanol, 20% glycerol, 6.5% hydrochloric acid, and 3.5% nitric acid in volume percent was applied to Ni; a solution of 70% methanol, 20% glycerol, and 10% perchloric acid in volume percent was applied to CoCrNi) to remove any work-hardened surface layer that may affect the incipient plasticity [1].

The X-ray diffraction (XRD, PANalytical AERIS) and electron back scattering diffraction (EBSD, JEOL JSM-7100F) were performed to characterize the phase structure and grain orientation. A nanoindentation instrument (Bruker, Minneapolis, MN, USA) with a Berkovich tip (radius of ~ 273 nm) was used to perform pop-in tests. Prior to the experiments, the tip radius was calibrated on a reference fused quartz sample. Pop-in behavior was studied with a maximum load of 200 μN and a fixed loading rate of 40 $\mu N/s$. More than 400 tests were performed on each sample with a 5- μm interval. To avoid the lattice-orientation interference, all tests were conducted on (001) planes.

The XRD patterns and EBSD images of Ni-w, Ni-f, CoCrNi-w, and CoCrNi-f are displayed in Fig. 1, showing a single face-centered-cubic (FCC) crystal structure, accompanied by equiaxed crystallites, and their grain sizes are 190, 237, 198 and 210 μm . The lattice constants, a, of Ni and CoCrNi are ~ 3.53 and ~ 3.56 Å, respectively. According to the Hertzian contact framework [25], the elastic segment before the first pop-in on each P-h curve can be depicted by:

$$P = \frac{4}{3}E_{\rm r}\sqrt{Rh^3} \tag{1}$$

where $E_{\rm r}$ is the reduced modulus, and R the tip radius of the indenter. Statistics of P- $h^{3/2}$ pairs at the first pop-in is displayed in Fig. 2a. After linear fitting, the reduced moduli, $E_{\rm r}$, can be derived as ~ 182 and ~ 218 GPa for Ni and CoCrNi, respectively. Combined with the Poisson's ratio, ν , values measured by an ultrasonic pulse-echo technique, the elastic moduli, $E_{\rm r}$, and the shear moduli, $E_{\rm r}$, are ~ 197 and ~ 76 GPa for Ni, and ~ 243 and ~ 93 GPa for CoCrNi, respectively. From these results, the maximum shear stress, $\tau_{\rm max}$, at the first pop-in can be calculated by Ref. [25]:

$$\tau_{\text{max}} = \frac{0.47}{\pi} \left(\frac{4E_{\text{r}}}{3R} \right)^{2/3} P^{1/3} \tag{2}$$

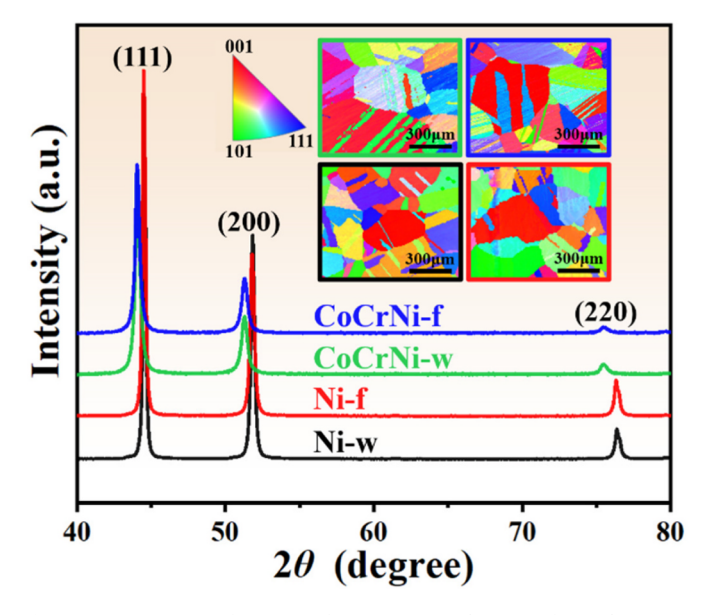


Fig. 1. XRD patterns of Ni-w, Ni-f, CoCrNi-w, and CoCrNi-f samples. EBSD images are marked with the same color border in the upper right corner. (For interpretation of the references to color in this figure legend, the reader is referred to the Web version of this article.)

The $\tau_{\rm max}$ data of the incipient plasticity conducted on the (001) surfaces, as a function of the cumulative probability, F, are plotted in Fig. 2b. It is intuitive from this figure that the $\tau_{\rm max}$ values of Ni-w and Ni-f possess an outstanding coincidence. However, there is a stark separation between CoCrNi-w and CoCrNi-f. The detailed cumulative distribution of $\tau_{\rm max}$, including the maximum, minimum, mean, standard deviation (SD), and CoV (defined as the ratio of the standard deviation and the mean), is summarized in Table 1. All cumulative distributions described by SD and CoV have similar distribution properties. Furthermore, the slow cooling, originating from furnace cooling, significantly enhances the critical stress for the incipient plasticity of CoCrNi. Referring to the temperature dependence of the site preferences of atoms, furnace cooling offers the possibility of the local atomic rearrangement, that is, promotes the generation of SROs. The existence of the SRO structure will strengthen the alloys [26].

Fig. 3 demonstrates the histograms of the density distributions of τ_{max} for Ni-w, Ni-f, CoCrNi-w, and CoCrNi-f. There is a "shoulder" or asymmetry in each density distribution [19,27]. Concomitantly, the kernel density estimates (KDEs) are executed, as seen in Fig. 3 [22–24]. For the deconvolution of the density distributions, a Gaussian statistical model [28,29] is employed, described as:

$$f(\tau_{\text{max}}) = \frac{1}{\sigma\sqrt{2\pi}} exp\left(-\frac{(\tau_{\text{max}} - \overline{\tau_{\text{max}}})^2}{2\sigma^2}\right)$$
(3)

where σ represents standard deviation. Correspondingly, the deconvolution results, which exhibit a bimodal distribution, are presented in Fig. 3. Peaks 1 and 2 correspond to low-intensity and high-intensity peaks, respectively. The Gaussian distribution deconvolution results, including the mean $(\overline{\tau_{max}})$, ratio to shear modulus $(\overline{\tau_{max}}/G)$, and areal fraction of each peak (AF), are listed in Table 2. Clearly, furnace cooling promotes an increase in the proportion of low-intensity peaks, compared to the case where high-intensity peaks dominate in the water-quenching condition. In addition, slow cooling also drives each deconvoluted peak to the right by an inconsistent offset.

With respect to each deconvoluted peak, the relationship between F and τ_{max} , to estimate the activation volume, V, of incipient plasticity, is described as follows [20,30,31]:

$$\ln[-\ln(1-F)] = \frac{V}{kT}\tau_{\text{max}} + \beta \tag{4}$$

where k is the Boltzmann constant, T is the absolute temperature, and the parameter, β , is of weak P dependence. By plotting $\ln[-\ln(1-F)]$ versus $\tau_{\rm max}$ for each of the deconvoluted peaks in Fig. 4, V can be calculated from the slope, and the results are annotated near each peak in Fig. 3. Here, V is normalized to the value of the atomic volume, Ω (= $0.25a^3$ for the FCC structure). For Ni-w and Ni-f, V is less than 1 Ω for Peak 1 and greater than 1 Ω for Peak 2. In this case, CoCrNi-w maintains the same trend, while CoCrNi-f does the opposite.

For incipient plasticity, there are generally two dislocation behaviors involved, dislocation nucleation or the slip of the pre-existing mobile dislocations [32,33]. The latter can be excluded, since the small critical resolved shear stress for dislocation slip and large dislocation spacing [34,35] (it is about $\sim 1~\mu m$ in a fully-annealed sample). Therefore, dislocation nucleation is the only possible mechanism for the elastoplastic transition due to the low probability of encountering pre-existing dislocations.

When it comes to the dislocation-nucleation mechanism, both homogeneous and heterogeneous modes need to be discussed. Considering the homogeneous nucleation, the activation volume, V, is carried out on the order of the atomic sizes and is usually smaller than 1 Ω [35]. Meanwhile, the critical shear stress of the first pop-in is high, that is, close to the theoretical shear strength [22]. Compared to other works, what needs to be noticed here is the effect of loading rate on $\tau_{\rm max}$, i.e., a high loading rate leads to a high intensity value [18,36–38]. Considering these factors, it is largely plausible that Peak 2 is inferred to be

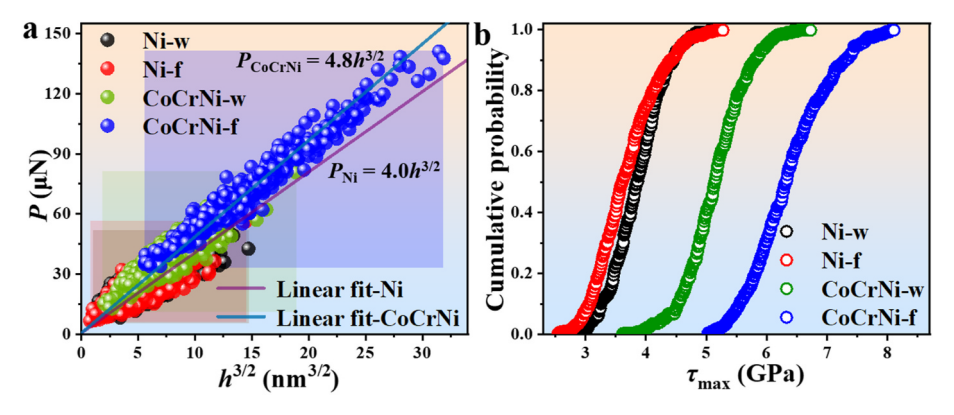


Fig. 2. (a) Statistics of at least 400 P- $h^{3/2}$ pairs at first pop-ins and (b) cumulative probability distributions of τ_{max} for the tests of Ni-w, Ni-f, CoCrNi-w, and CoCrNi-f samples.

Table 1 Summary of minimum, maximum, range, mean $(\overline{\tau_{max}})$, standard deviation (SD), and CoV values of τ_{max} for each sample.

	$ au_{max}(GPa)$						
	Min.	Max.	Range	$\overline{ au_{ ext{max}}}$	SD	CoV	
Ni-w	2.76	5.12	2.36	3.86	0.44	11%	
Ni-f	2.55	5.29	2.74	3.68	0.52	14%	
CoCrNi-w	3.61	6.73	3.12	5.15	0.51	10%	
CoCrNi-f	5.03	8.11	3.08	6.38	0.65	10%	

dominated by the homogeneous dislocation nucleation from a defect-free zone. Correspondingly, Peak 1 is mainly caused by the heterogeneous dislocation nucleation from the pre-existing defects, such as vacancies, vacancy clusters, and impurities.

On the above basis, we ascribe the heterogeneous nucleation to the role of a definite type of defects. To reveal the defect type leading to the heterogeneous nucleation of dislocations, the defect density is calculated here. First and foremost, it needs to be assumed that a pop-in will occur if and only if there is at least one defect within a representative volume, V_s , of the stressed material under the indenter. Then, Poisson's (or exponential) statistics are employed to estimate the probability for the existence of such a defect, P_{low} , as follows [23,39]:

$$P_{\text{low}} = 1 - exp(-\rho_{\text{low}}V_s) \tag{5}$$

where ρ_{low} is the defect density per unit volume, and the P_{low} is taken as the areal fraction of low intensity peaks (in Table 2). As for V_{s} , the assumption of Mason et al. is adopted [21], that is, $V_{\mathrm{s}}=\pi a_{\mathrm{c}}^3$, where a_{c} is the contact radius.

Due to the shallow depth of the first pop-in for the four samples, the part of the indenter tip in contact with the sample surface can be approximated as a spherical indenter with a radius of ~ 273 nm, over the entire distribution range of h ($h \le 11$ nm), so: $a_{\rm c} = \left(\frac{3PR}{4E_{\rm r}}\right)^{1/3}$ [40]. By inputting the experimental data into Eq. (5), $\rho_{\rm low}$ is estimated as \sim $1.67\text{--}17.29\times10^3~\mu\text{m}^{-3}.$ In turn, the average spacings between defects, $l = 1/\sqrt[3]{\rho_{\text{low}}}$, are 84.3, 42.9, 83.3, and 45.4 nm for Ni-w, Ni-f, CoCrNi-w, and CoCrNi-f, respectively. Meanwhile, the vacancy concentration is estimated to be 10^{-6} in a thermal equilibrium at room temperature [19]. The average vacancy spacing, $l_{\rm vac}$, of Ni and CoCrNi is \sim 22 nm (= $(10^6 \div \text{atoms per unit cell})^{1/3} \times a$), which is similar to the above-mentioned l value. From this trend, it can be speculated that vacancies are most likely to dominate heterogeneous nucleation through the monovacancy-mediated dislocation nucleation. The possible reasons why l and l_{vac} are not exactly equal are: (a) The relative positions of the vacancy site and the indenter affect the critical resolved shear stress for the nucleation of dislocations on different slip planes. (b) The uneven

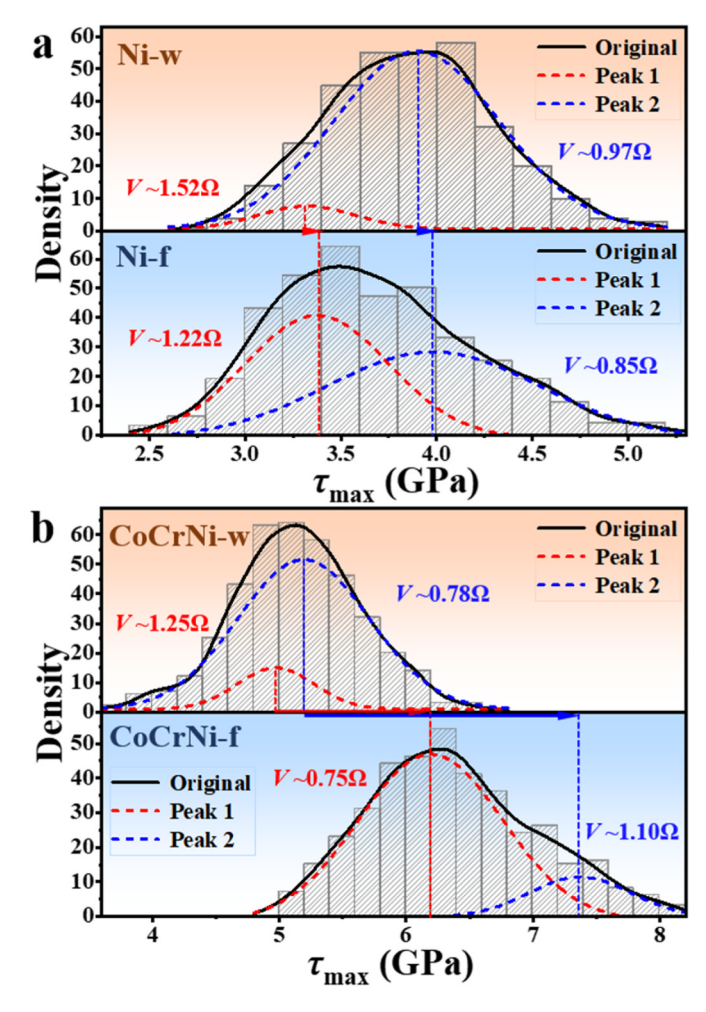


Fig. 3. Histograms, KDE curves and deconvolution results by Gaussian distributions for the tests of Ni-w, Ni-f, CoCrNi-w, and CoCrNi-f samples. The V of each peak is also given in terms of Ω , and the dashed line marks the average $\tau_{\rm max}$ value of each peak.

distribution of forces within the V_s , which makes it difficult for the stress values at the vacancies in the edge regions of the V_s to reach the critical stress for dislocation nucleation. Both cases will lead to an underestimation of the vacancy concentration.

As for the activation volume, V, of Ni and CoCrNi marked in Fig. 3, Ni-w, Ni-f, and CoCrNi-w show the same trend, that is, the V of Peak 1 (heterogeneous nucleation) is greater than 1 Ω , while that of Peak 2

Table 2The results of deconvolution by Gaussian distribution.

	Peak	$\overline{ au_{ ext{max}}}$ (GPa)	$\overline{ au_{ ext{max}}}$ /G	AF
Ni-w	1	3.32	1/23	0.08
	2	3.90	1/19	0.92
Ni-f	1	3.38	1/22	0.49
	2	3.98	1/19	0.51
CoCrNi-w	1	4.97	1/19	0.15
	2	5.19	1/18	0.85
CoCrNi-f	1	6.19	1/15	0.86
	2	7.37	1/13	0.14

(homogeneous nucleation) is less than 1 Ω . For CoCrNi-f, unexpectedly, the opposite trend appears in Fig. 3b. Based on the current theoretical basis and detection methods, there are still obstacles to revealing this opposite trend. After a detailed comparison, this opposite trend is absolutely inseparable from the role of SRO, although no similar trend is suggested.

Driven by the inequable cooling rates, the non-uniform residualstress distribution will be formed inside the samples. Compared with furnace cooling, rapid cooling makes the residual stress in the material more evident. In Fig. 3a, the discrepancy in density distributions of τ_{max} of Ni-w and Ni-f provides an indispensable basis for the separation treatment of residual-stress effects. Based on Ni-w, Peaks 1 and 2 for Ni-f are shifted to the right by \sim 0.07 GPa, and the strength of the material rises slightly. As a consequence, the residual stress induced by rapid cooling reduces the au_{max} of dislocation nucleation, that is, the residual stress can function as a booster for dislocation nucleation. When referring to the V, it is suggested that the release of the residual stress will make the V smaller. Moreover, the proportion of Peak 1 of Ni-f (~ 0.49) is larger than that of Ni-w (~ 0.08) with an increment of 0.41, which is most likely due to the fact that the homogeneous dislocation nucleation in Ni-f is harder to initiate after τ_{max} is enhanced. For CoCrNi, the proportion of Peak 1 increases from 0.15 to 0.86 with decreasing the cooling rate. The more significant proportional increase comes from the combined action of the residual stress and SROs. It is therefore of supreme importance to point out the exact reinforcement effect of SROs.

From Fig. 3b, Peaks 1 and 2 of CoCrNi-f are noted to both shift to higher stress values with larger increments due to the slow cooling rate. Compared to the smaller strength increment in Ni induced by the weakening of the residual stress, the strengthening effect of SROs has to be highlighted. As is the case here, some related studies have also shown that the presence of SROs in HEAs/MEAs induces higher overall lattice frictional resistance to dislocation motion, which results in the improved alloy strength [41,42]. According to the characterization of SROs in other works [1,2,15], it is assumed that the degree of SRO in CoCrNi-f is at a similar level, that is, its size is between \sim 0.60–1.13 nm, and its areal fraction is between \sim 18% and 25%. From this trend, the density of SRO (ρ_{SRO}) is estimated to be ~ 1.79 – $8.84 \times 10^5 \, \mu m^{-2}$, and its mean interval $(l_{\rm SRO}=1/\sqrt{\rho_{\rm SRO}})$ is ~ 1.06 –2.36 nm. Understandably, high-density SRO in the V_s will bring a significant strengthening effect. With the assumption that the residual stress has a comparable effect on the $\tau_{\rm max}$ of different dislocation nucleation mechanisms in Ni and CoCrNi. Hence, it is inferred that the τ_{max} values of Peak 1 and 2 of CoCrNi increases by 22.4% and 39.9% due to SROs, respectively. Given the more remarkable strengthening effect of SROs, the proportion of Peak 1 increases from 0.15 to 0.86 is fully explainable, stemming from the fact that dislocation nucleation becomes more difficult to proceed as $\tau_{\rm max}$ increases.

To sum up, slow cooling after the homogenization treatment significantly improved the incipient plastic strength of CoCrNi due to SROs. Compared with pure Ni, it is suggested that the residual stress induced by rapid cooling play only a minor role. Furthermore, they are SROs in CoCrNi that strengthen the alloy more prominently, which originates from the effect of processing conditions such as cooling rate. Therefore, adjusting the size and volume fraction of SROs, by changing the annealing process and cooling method, is an effective way to strengthen the multi-principal elements alloys.

Originality statement

I write on behalf of myself and all co-authors to confirm that the results reported in the manuscript are original and neither the entire

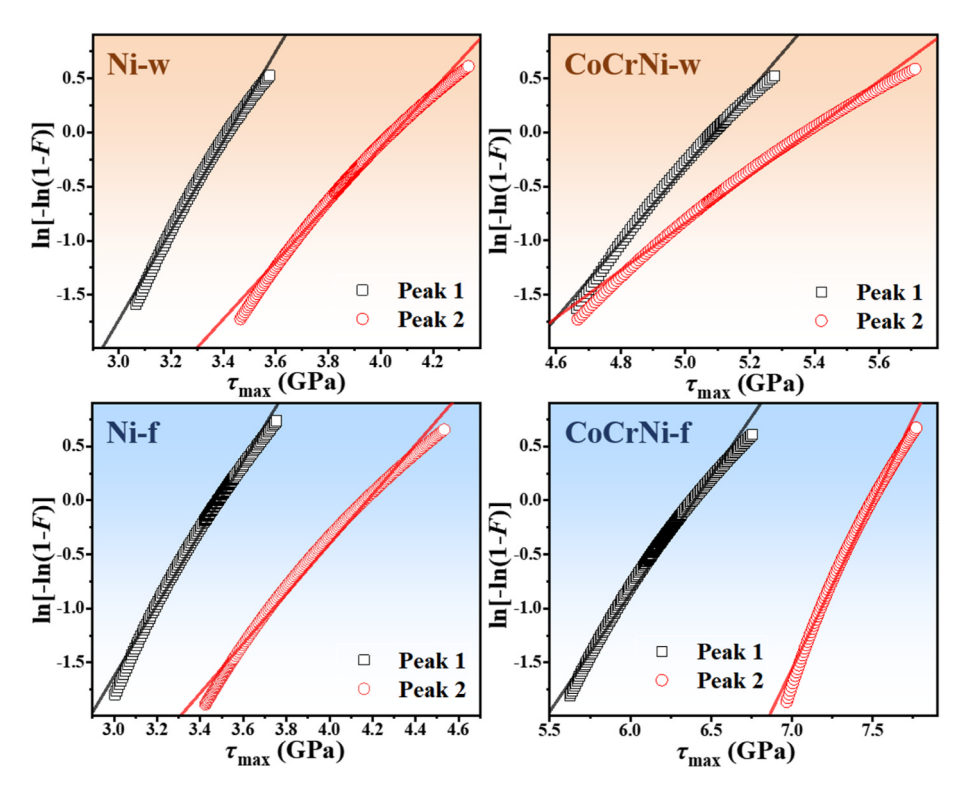


Fig. 4. Plot of $\ln[-\ln(1-F)]$ vs $P^{1/3}$ to determine the activation volume from each peak of Ni-w, Ni-f, CoCrNi-w, and CoCrNi-f samples.

work, nor any of its parts have been previously published. The authors confirm that the article has not been submitted to peer review, nor has been accepted for publishing in another journal. The author(s) confirms that the research in their work is original, and that all the data given in the article are real and authentic. If necessary, the article can be recalled, and errors corrected.

CRediT authorship contribution statement

Q. Zhang: Conceptualization, Data curation, Writing – original draft. **X. Jin:** Software, Writing – review & editing. **X.H. Shi:** Resources, Data curation. **J.W. Qiao:** Conceptualization, Writing – review & editing, Project administration. **P.K. Liaw:** Writing – review & editing.

Declaration of competing interest

The authors declare that they have no known competing financial interests or personal relationships that could have appeared to influence the work reported in this paper.

Data availability

Data will be made available on request.

Acknowledge

The authors would like to acknowledge the financial support of the Natural Science Foundation of Shanxi Province, China (Nos. 201901D111105 and 201901D111114), and Key Research and Development Program of Shanxi Province (No. 202102050201008). PKL very much appreciates the supports from the National Science Foundation (No. DMR-1611180 and 1809640) and the Army Research Office (No. W911NF-13-1-0438 and W911NF-19-2-0049).

Appendix A. Supplementary data

Supplementary data to this article can be found online at https://doi. org/10.1016/j.msea.2022.143890.

References

- [1] R. Zhang, S. Zhao, J. Ding, Y. Chong, T. Jia, C. Ophus, M. Asta, R.O. Ritchie, A M. Minor, Nature 581 (7808) (2020) 283–287.
- [2] X. Chen, Q. Wang, Z. Cheng, M. Zhu, H. Zhou, P. Jiang, L. Zhou, Q. Xue, F. Yuan, J. Zhu, X. Wu, E. Ma, Nature 592 (7856) (2021) 712–716.
- [3] L.J. Santodonato, Y. Zhang, M. Feygenson, C.M. Parish, M.C. Gao, R.J.K. Weber, J. C. Neuefeind, Z. Tang, P.K. Liaw, Nat. Commun. 6 (2015) 5964.
- [4] S. Singh, N. Wanderka, B.S. Murty, U. Glatzel, J. Banhart, Acta Mater. 59 (1) (2011) 182–190.
- [5] E. Antillon, C. Woodward, S.I. Rao, B. Akdim, T.A. Parthasarathy, Acta Mater. 190 (2020) 29–42.

- [6] D.B. Miracle, O.N. Senkov, Acta Mater. 122 (2017) 448-511.
- [7] Q. Pan, L. Zhang, R. Feng, Q. Lu, K. An, A.C. Chuang, J.D. Poplawsky, P.K. Liaw, L. Lu, Science 374 (6570) (2021) 984–989.
- [8] P.J. Shi, R.G. Li, Y. Li, Y.B. Wen, Y.B. Zhong, W.L. Ren, Z. Shen, T.X. Zheng, J. C. Peng, X.L. Liang, P.F. Hu, N. Min, Y. Zhang, Y. Ren, P.K. Liaw, D. Raabe, Y. D. Wang, Science 373 (6557) (2021) 912–918.
- [9] W. Li, D. Xie, D. Li, Y. Zhang, Y. Gao, P.K. Liaw, Prog. Mater. Sci. 118 (2021).
- [10] Y. Zhang, T.T. Zuo, Z. Tang, M.C. Gao, K.A. Dahmen, P.K. Liaw, Z.P. Lu, Prog. Mater. Sci. 61 (2014) 1–93.
- [11] Q. Ding, Y. Zhang, X. Chen, X. Fu, D. Chen, S. Chen, L. Gu, F. Wei, H. Bei, Y. Gao, M. Wen, J. Li, Z. Zhang, T. Zhu, R.O. Ritchie, Q. Yu, Nature 574 (7777) (2019) 223–227.
- [12] F.X. Zhang, S. Zhao, K. Jin, H. Xue, G. Velisa, H. Bei, R. Huang, J.Y.P. Ko, D. C. Pagan, J.C. Neuefeind, W.J. Weber, Y. Zhang, Phys. Rev. Lett. 118 (20) (2017), 205501
- [13] S. Bajpai, B.E. MacDonald, T.J. Rupert, H. Hahn, E.J. Lavernia, D. Apelian, Materialia 24 (2022), 101476.
- [14] B. Wu, Y. Zhao, H. Ali, R. Chen, H. Chen, J. Wen, Y. Liu, L. Liu, K. Yang, L. Zhang, Z. He, Q. Yao, H. Zhang, B. Sa, C. Wen, Y. Qiu, H. Xiong, M. Lin, Y. Liu, C. Wang, H. Su, Intermetallics 144 (2022).
- [15] D. Liu, Q. Wang, J. Wang, X.F. Chen, P. Jiang, F.P. Yuan, Z.Y. Cheng, E. Ma, X. L. Wu, Mater. Today Nano 16 (2021), 100139.
- [16] B. Yin, S. Yoshida, N. Tsuji, W.A. Curtin, Nat. Commun. 11 (1) (2020).
- [17] E. Ma, Scripta Mater. 181 (2020) 127-133.
- [18] S.I. Hong, J. Moon, S.K. Hong, H.S. Kim, Mater. Sci. Eng., A 682 (2017) 569-576.
- [19] C. Zhu, Z.P. Lu, T.G. Nieh, Acta Mater. 61 (8) (2013) 2993-3001.
- [20] Y.X. Ye, Z.P. Lu, T.G. Nieh, Scripta Mater. 130 (2017) 64-68.
- [21] J.K. Mason, A.C. Lund, C.A. Schuh, Phys. Rev. B 73 (5) (2006), 054102.
- Y. Zhao, J.-M. Park, J.-i. Jang, U. Ramamurty, Acta Mater. 202 (2021) 124–134.
 J.H. Perepezko, S.D. Imhoff, M.-W. Chen, J.-Q. Wang, S. Gonzalez, PNAS 111 (11) (2014) 3938–3942.
- [24] S. Nag, R.L. Narayan, J.-i. Jang, C. Mukhopadhyay, U. Ramamurty, Scripta Mater. 187 (2020) 360–365.
- [25] K.L. Johnson, Cambridge University Press, 1985.
- [26] Y. Wu, F. Zhang, X. Yuan, H. Huang, X. Wen, Y. Wang, M. Zhang, H. Wu, X. Liu, H. Wang, S. Jiang, Z. Lu, J. Mater. Sci. Technol. 62 (2021) 214–220.
- [27] S. Mridha, M. Sadeghilaridjani, S. Mukherjee, Metals 9 (2) (2019) 263.
- [28] T.L. Li, Y.F. Gao, H. Bei, E.P. George, J. Mech. Phys. Solid. 59 (6) (2011) 1147–1162.
- [29] Y. Gao, H. Bei, Prog. Mater. Sci. 82 (2016) 118-150.
- [30] G. Yang, Y. Zhao, D.-H. Lee, J.-M. Park, M.-Y. Seok, J.-Y. Suh, U. Ramamurty, J.-I. Jang, Scripta Mater. 161 (2019) 23–27.
- [31] Y.X. Ye, B. Ouyang, C.Z. Liu, G.J. Duscher, T.G. Nieh, Acta Mater. 199 (2020) 413–424.
- [32] H. Bei, Y.F. Gao, S. Shim, E.P. George, G.M. Pharr, Phys. Rev. B 77 (6) (2008), 060103.
- [33] A. Montagne, V. Audurier, C. Tromas, Acta Mater, 61 (13) (2013) 4778–4786.
- [34] N.L. Okamoto, S. Fujimoto, Y. Kambara, M. Kawamura, Z.M.T. Chen, H. Matsunoshita, K. Tanaka, H. Inui, E.P. George, Sci. Rep. 6 (2016), 35863.
- [35] K. Gan, D. Yan, S. Zhu, Z. Li, Acta Mater. 206 (2021), 116633.
- [36] C.A. Schuh, A.C. Lund, J. Mater. Res. 19 (7) (2011) 2152-2158.
- [37] Y. Wang, W. Liu, Y. Ma, Y. Huang, Y. Tang, H. Luo, Q. Yu, Mater. Lett. 131 (2014) 57–60.
- [38] Y. Zhao, X. Wang, T. Cao, J.-K. Han, M. Kawasaki, J.-i. Jang, H.N. Han, U. Ramamurty, L. Wang, Y. Xue, Mater. Sci. Eng., A 782 (2020), 139281.
- [39] P.S. Phani, K.E. Johanns, E.P. George, G.M. Pharr, J. Mater. Res. 28 (19) (2013) 2728–2739.
- [40] J.R. Morris, H. Bei, G.M. Pharr, E.P. George, Phys. Rev. Lett. 106 (16) (2011), 165502.
- [41] L. Zhang, Y. Xiang, J. Han, D.J. Srolovitz, Acta Mater. 166 (2019) 424-434.
- [42] F. Cao, Y. Wang, L. Dai, Acta Mater. 194 (2020) 283–294.